

DATA REPOSITORY

Table DR1. LA-ICPMS isotopic U-Pb and trace element concentration data

METHODS FOR U-PB GEOCHRONOLOGY ON ZIRCON

Zircon grains were separated from rock crushed with a SelFrag (Wang et al., 2012) using standard techniques and annealed at 900 °C for 60 h in a muffle furnace. Zircon grains were separated in a faceted fraction and a round fraction, assuming that the faceted zircon grains are more likely to be younger and are better candidates to constraint the maximum age of deposition. All 29 faceted grains and ~200 randomly selected round grains were mounted in epoxy and polished until their centers were exposed. Cathodoluminescence (CL) images were obtained with a JEOL JSM-1300 scanning electron microscope and Gatan MiniCL. Zircon was analyzed by laser ablation inductively coupled plasma mass spectrometry (LA-ICPMS) using a ThermoElectron X-Series II quadrupole ICPMS and New Wave Research UP-213 Nd:YAG UV (213 nm) laser ablation system at Boise State University. In-house analytical protocols, standard materials, and data reduction software were used for acquisition and calibration of U-Pb dates and a suite of high field strength elements (HFSE) and rare earth elements (REE). Zircon was ablated with a laser spot of 25 μm wide using fluence and pulse rates of 5 J/cm^2 and 10 Hz, respectively, during a 45 second analysis (15 s gas blank, 30 s ablation) that excavated a pit ~25 μm deep. Ablated material was carried by a 1.2 L/min He gas stream to the nebulizer flow of the plasma. Quadrupole dwell times were 5 ms for Si and Zr, 200 ms for ^{49}Ti and ^{207}Pb , 80 ms for ^{206}Pb , 40 ms for ^{202}Hg , ^{204}Pb , ^{208}Pb , ^{232}Th , and ^{238}U and 10 ms for all other HFSE and REE; total sweep duration is 950 ms. Background count rates for each analyte were obtained prior to each spot analysis and subtracted from the raw count rate for each analyte. For concentration calculations, background-subtracted count rates for each analyte were internally normalized to ^{29}Si and calibrated with respect to NIST SRM-610 and -612 glasses as the primary standards. Ablations pits that appear to have intersected glass or mineral inclusions were identified based on Ti and P signal excursions, and associated sweeps were discarded. U-Pb dates from these analyses are considered valid if the U-Pb ratios appear to have been unaffected by the inclusions. Signals at mass 204 were normally indistinguishable from zero following subtraction of mercury backgrounds measured during the gas blank (<1000 cps ^{202}Hg), and thus dates are reported without common Pb correction. Rare analyses that appear contaminated by common Pb were rejected based on mass 204 greater than baseline.

Data were collected in two experiments on the faceted and round grains, respectively. For U-Pb and $^{207}\text{Pb}/^{206}\text{Pb}$ dates, instrumental fractionation of the background-subtracted ratios was corrected and dates were calibrated with respect to interspersed measurements of zircon standards and reference materials. The primary standard Plešovice zircon (Sláma et al., 2008) was used to monitor time-dependent instrumental fractionation based on two analyses for every 10 analyses of unknown zircon. A secondary correction to the $^{206}\text{Pb}/^{238}\text{U}$ dates was made based on results from the zircon standards Seiland (530 Ma, personal communication, Isotope Geology

Laboratory, Boise State University, 2009) and Zirconia (327 Ma, personal communication, Isotope Geology Laboratory, Boise State University, 2009), which were treated as unknowns and measured once for every 10 analyses of unknown zircon. These results showed a linear age bias of 0%–4% that is related to the ^{206}Pb count rate. The secondary correction is thought to mitigate matrix-dependent variations due to contrasting compositions and ablation characteristics between the Plešovice zircon and other standards (and unknowns).

Radiogenic isotope ratio and age error propagation for all analyses includes uncertainty contributions from counting statistics and background subtraction. The error on the weighted mean calculation includes uncertainties from the standard calibrations during the two experiments. These uncertainties are the local standard deviations of the polynomial fits to the interspersed primary standard measurements versus time for the time-dependent, relatively larger U/Pb fractionation factor, and the standard errors of the means of the consistently time-invariant and smaller $^{207}\text{Pb}/^{206}\text{Pb}$ fractionation factor. These uncertainties are 1.5 and 1.6% (2σ) for $^{206}\text{Pb}/^{238}\text{U}$ and 0.3 and 0.4% (2σ) for $^{207}\text{Pb}/^{206}\text{Pb}$.

Age interpretations are based on $^{207}\text{Pb}/^{206}\text{Pb}$ dates for analyses with $^{206}\text{Pb}/^{238}\text{U}$ dates >1000 Ma and $^{206}\text{Pb}/^{238}\text{U}$ dates for analyses with $^{206}\text{Pb}/^{238}\text{U}$ dates <1000 Ma. Analyses with >20% positive discordance and >10% negative discordance are not considered. Errors on the dates from individual analyses are given at 2σ . Probability density plots of dates were constructed using Isoplot 3.0 (Ludwig, 2003).

REFERENCES CITED

- Ludwig, K.R., 2003, User's Manual for Isoplot 3.00: Berkeley, California, Berkeley Geochronology Center, 70 p.
- Sláma, J., Košler, J., Condon, D.J., Crowley, J.L., Gerdes, A., Hanchar, J.M., Horstwood, M.S.A., Morris, G.A., Nasdala, L., Norberg, N., Schaltegger, U., Schoene, B., Tubrett, M.N., and Whitehouse, M.J., 2008, Plešovice zircon — A new natural reference material for U–Pb and Hf isotopic microanalysis: *Chemical Geology*, v. 249, p. 1–35, <https://doi.org/10.1016/j.chemgeo.2007.11.005>.
- Wang, E., Shi, F., and Manlapig, E., 2012, Mineral liberation by high voltage pulses and conventional comminution with same specific energy levels: *Minerals Engineering*, v. 27–28, p. 28–36, <https://doi.org/10.1016/j.mineng.2011.12.005>.

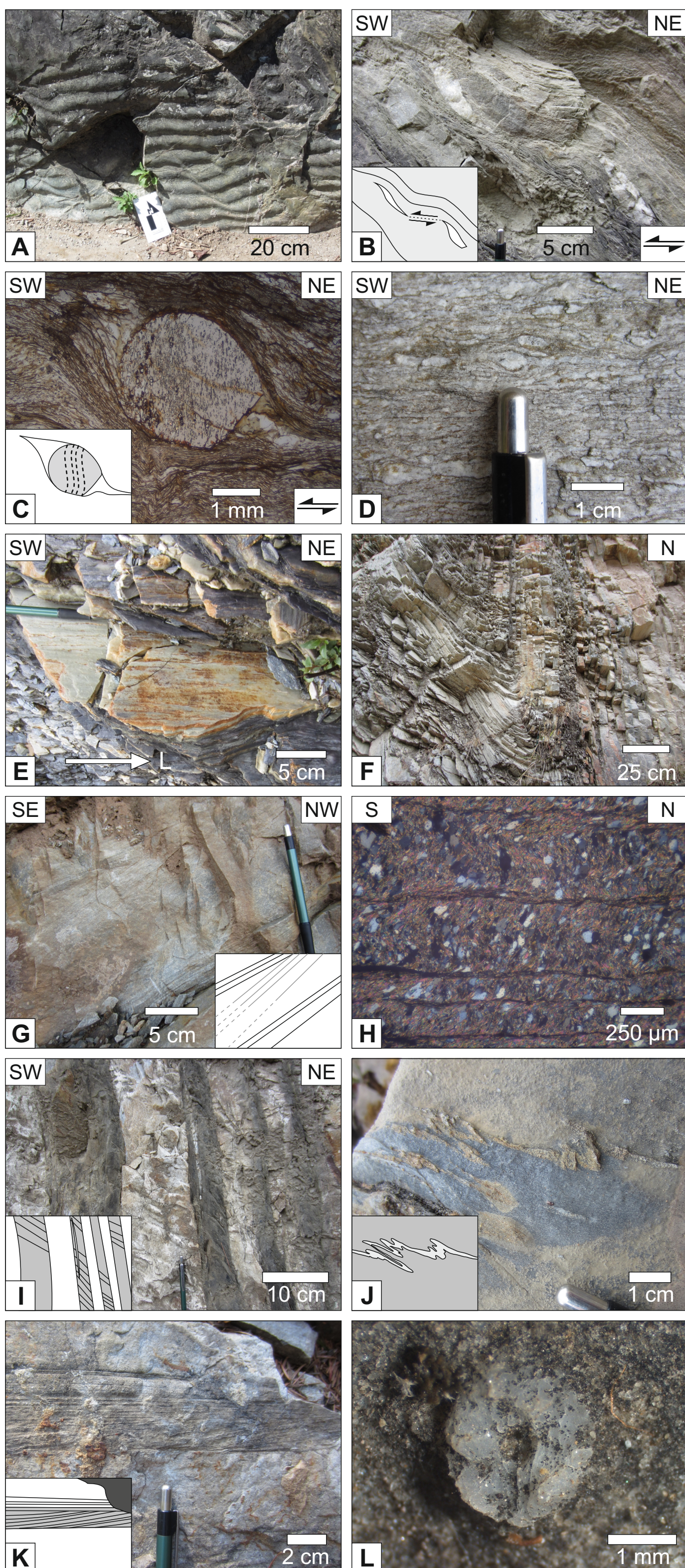


Figure DR1. High-resolution photographs of representative lithological units and structures in the Jajarkot klippe presented in Fig. 4. (A) Ripple marks in quartz arenite in the Nawakot Unit. (B) Asymmetric boudinaged quartz vein indicating top-to-the-southwest sense of shear at the base of the Jajarkot klippe. (C) Sigmoidal inclusion trails in a garnet porphyroblast with asymmetric pressure shadows indicating top-to-the-southwest sense of shear in the lower part of the Chaurjhari Unit. Microphotograph in cross-polarized light. (D) Granitic augen gneiss at the top of the Kuncha Unit. (E) Lineated quartzite of the Kuncha Unit. (F) Folds axial planar to the regional foliation in quartzite of the Kuncha Unit. (G) Cross-bed stratification (grey lines in inset) in arenite of the Thabang Unit. (H) Bedding-parallel crenulation cleavage transposing a perpendicular slaty cleavage preserved in microlithons of a muscovite-biotite schist of the Thabang Unit. (I) Interlayered marble (white) and biotite-muscovite schist (dark grey) of the Thabang Unit on the north flank of the klippe. A moderately dipping cleavage, interpreted to be axial planar to the regional synform, is developed only in the schist. The bedding-cleavage relationship implies that the north flank of the Jajarkot klippe is overturned along the easternmost transect. (J) Limestone and tightly folded beds of arenite in the Jaljala Unit. (K) Cross-bed stratification in arenite of the Jaljala Unit. (L) Crinoid ossicle in limestone of the Jaljala Unit.

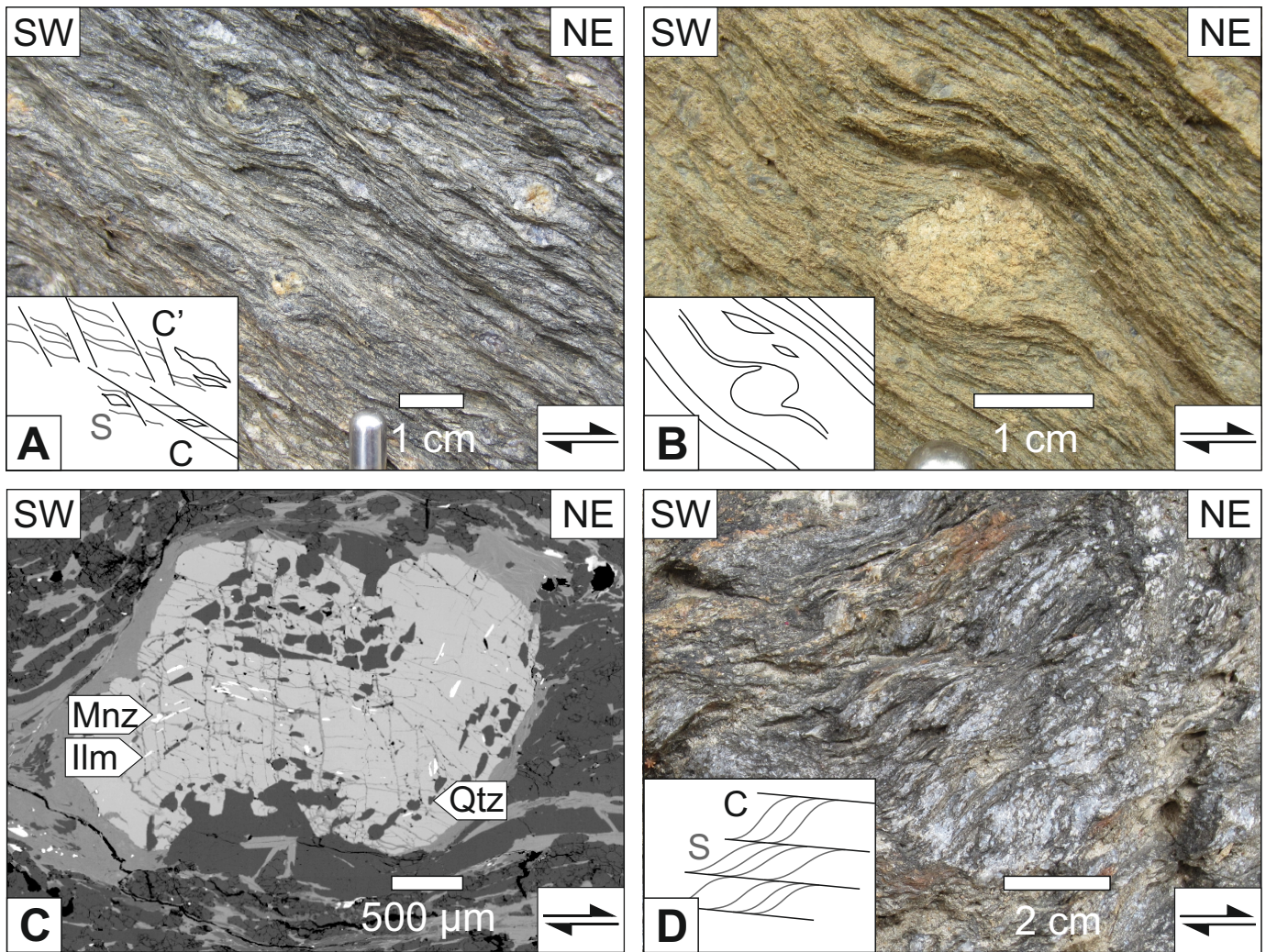


Figure DR2. High-resolution photographs of representative structures indicating top-to-the-northeast sense of shear at the contact between the Chaurjhari and Thabang Units presented in Fig. 5. (A) C-S-C' fabrics in a pebbly meta-arenite unit exposed along the Lungri Kholā transect. (B) δ -porphyroclast in the same pebbly meta-arenite unit. (C) Back scattered electron image of sigmoidal inclusion trails defined by ilmenite, quartz and monazite in garnet. (D) C-S fabric in a carbonaceous schist on the north flank of the western part of the klippe.

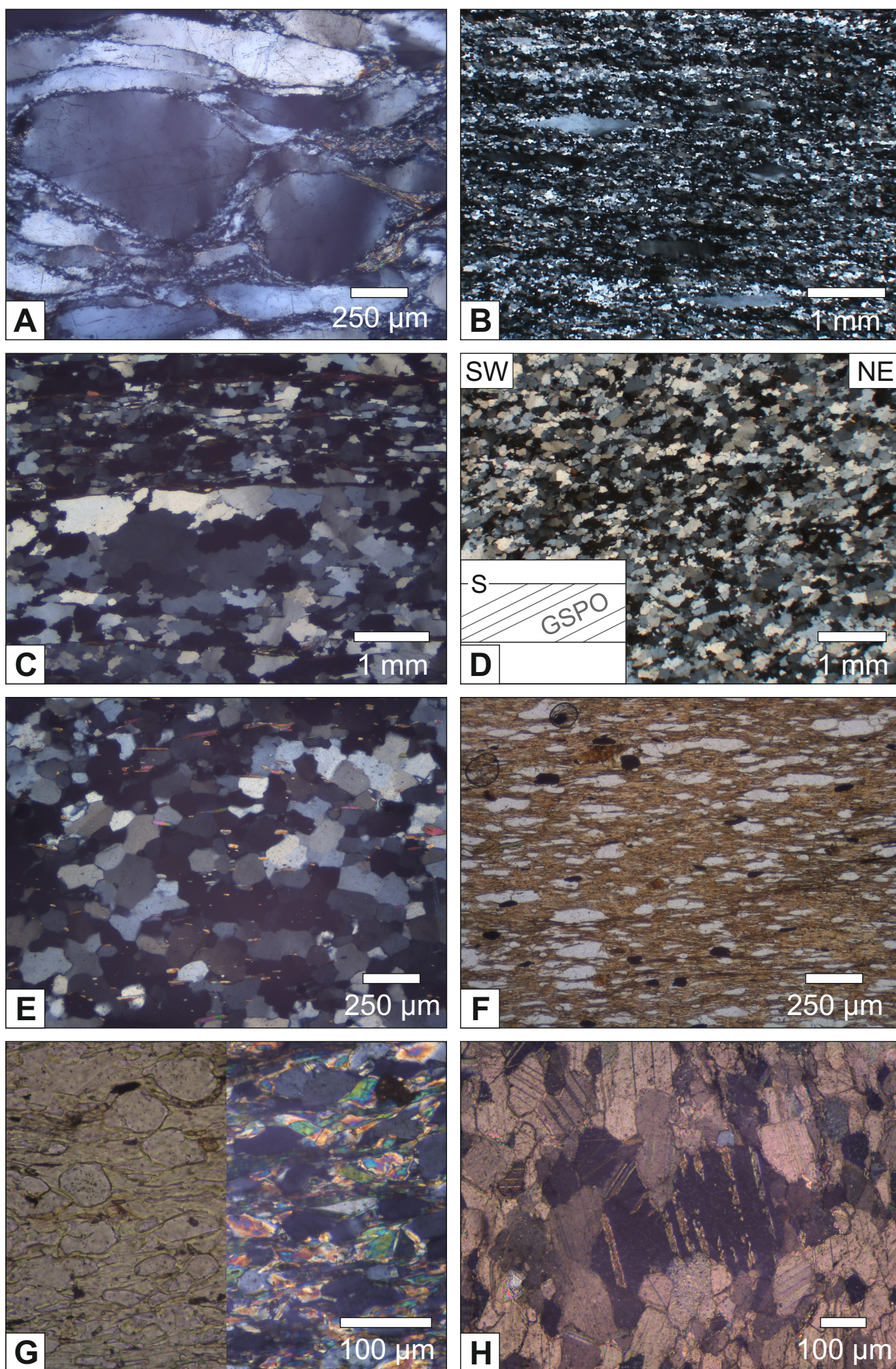


Figure DR3. High-resolution microphotographs in cross-polarized light, unless indicated otherwise, of representative quartz and calcite recrystallization microstructures presented in Fig. 6. (A) Bulging recrystallization at the edges of detrital quartz grains in the Nawakot Unit. (B) Dynamic recrystallization of quartz grains by subgrain rotation at the base of the Kuncha Unit. (C) Grain boundary migration in quartz grains from the base of the Chaurjhari Unit. (D) Grain boundary migration in quartz grains from the top of the Chaurjhari Unit. Quartz exhibit a grain shape preferred orientation (GSPO) oblique to the horizontal foliation indicating a top-to-the-northeast sense of shear. (E) Static recrystallization of quartz in the Chaurjhari Unit indicated by grain boundary area reduction. (F) Flattened detrital quartz grains in the Thabang Unit in plane polarized light. (G) Round detrital quartz grains in the Thabang formation with no evidence of dynamic or static recrystallization in plane polarized light (left) and cross-polarized light (right). (H) Calcite grains exhibit twin types II and IV in the Thabang Unit.

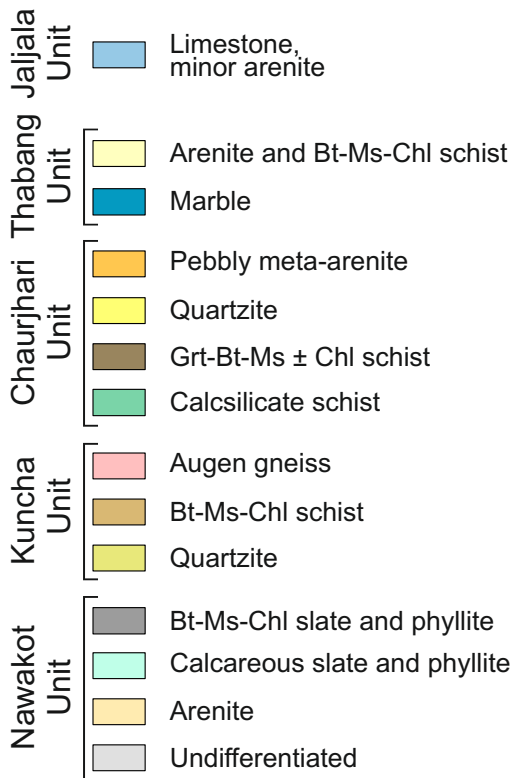
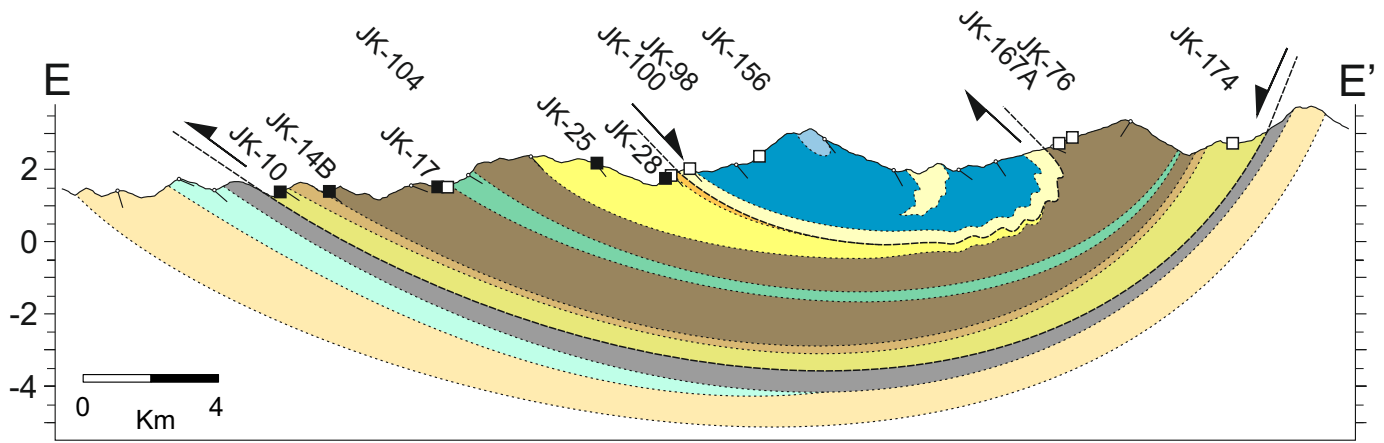
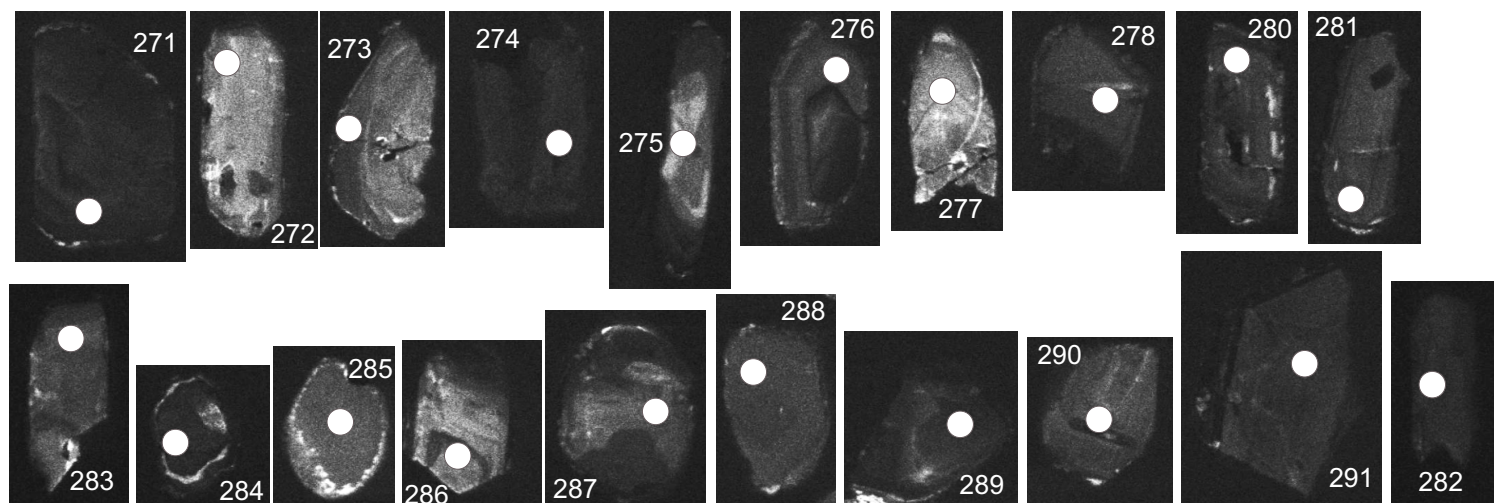


Figure DR4. Cross-section E-E' (located on Fig. 3) with the position of samples collected along the Lungri Kholā transect (bottom row, black rectangles) and the the projected position of the samples collected along other transects (top row, white rectangles).

JK-98 Faceted zircons



JK-98 Round zircons

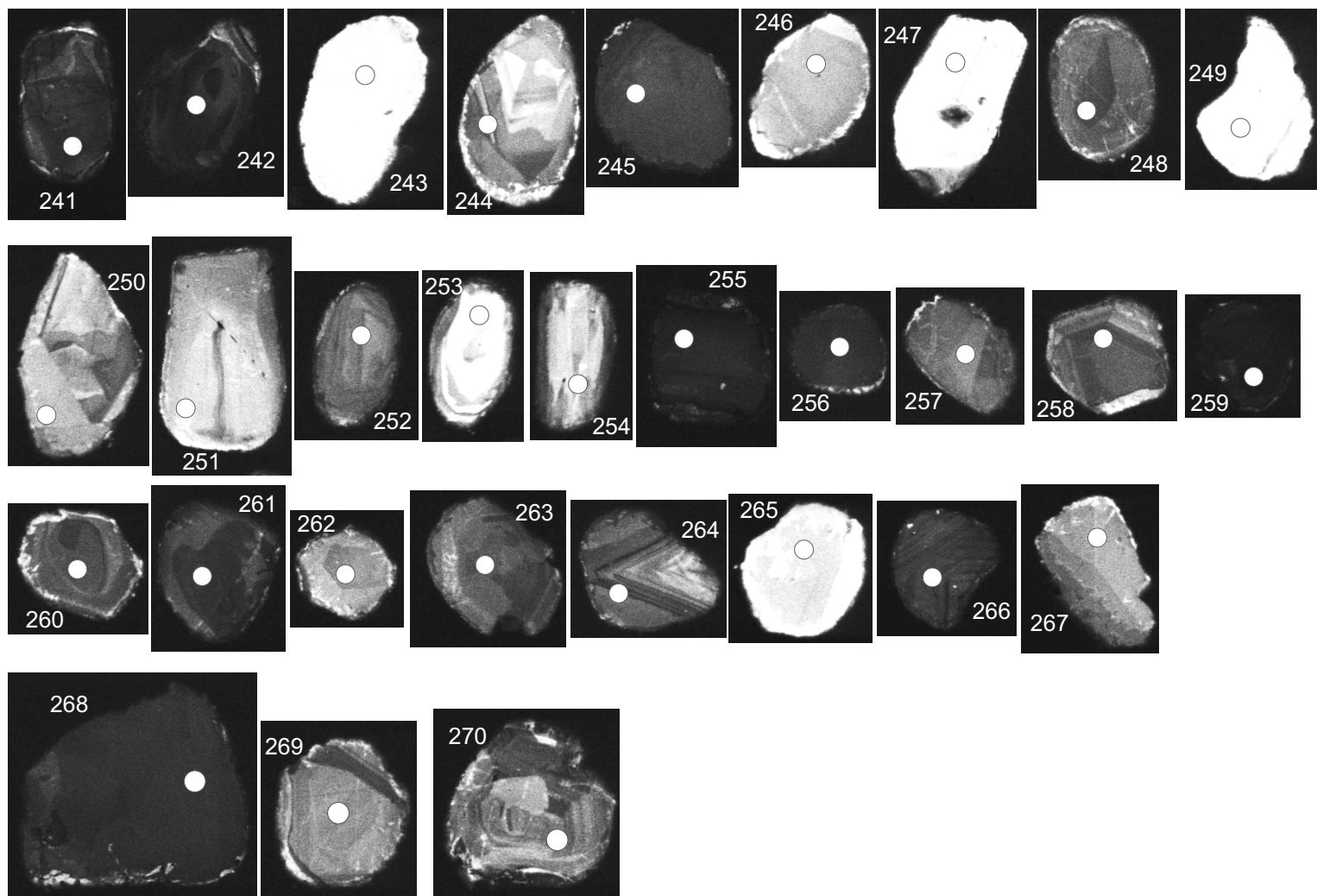


Figure DR5. Cathodoluminescence images of zircon with location and number of LA-ICPMS analyses.

*Fig. DR5. Soucy La Roche et al.
Reappraisal of emplacement models for Himalayan external crystalline nappes:
the Jajarkot klippe, western Nepal*

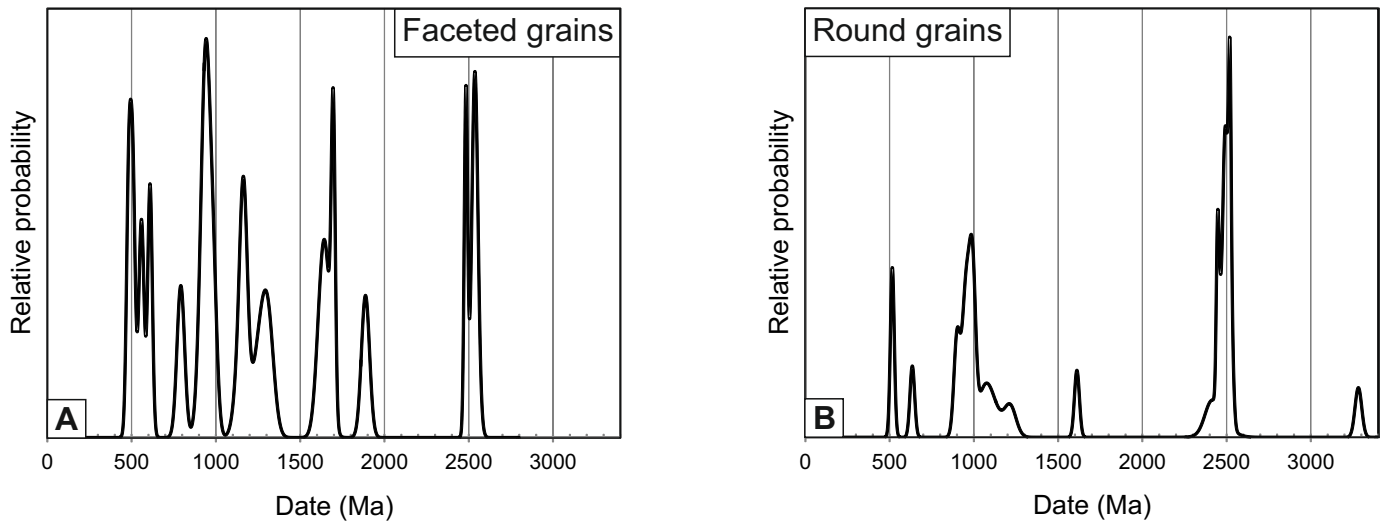


Figure DR6. Probability density plots of LA-ICPMS U-Pb zircon dates from sample JK-98 for (A) faceted grains and (B) round grains.